

## SOLAR CELLS

## Stabilizing black-phase formamidinium perovskite formation at room temperature and high humidity

Wei Hui<sup>1\*</sup>, Lingfeng Chao<sup>2\*</sup>, Hui Lu<sup>1\*</sup>, Fei Xia<sup>1</sup>, Qi Wei<sup>3</sup>, Zhenhuang Su<sup>4</sup>, Tingting Niu<sup>2</sup>, Lei Tao<sup>1</sup>, Bin Du<sup>1</sup>, Deli Li<sup>2</sup>, Yue Wang<sup>2</sup>, He Dong<sup>2</sup>, Shouwei Zuo<sup>5</sup>, Bixin Li<sup>6</sup>, Wei Shi<sup>1</sup>, Xueqin Ran<sup>1</sup>, Ping Li<sup>1</sup>, Hui Zhang<sup>1</sup>, Zhongbin Wu<sup>2</sup>, Chenxin Ran<sup>2</sup>, Lin Song<sup>2</sup>, Guichuan Xing<sup>3</sup>, Xingyu Gao<sup>4</sup>, Jing Zhang<sup>5</sup>, Yingdong Xia<sup>1</sup>, Yonghua Chen<sup>1†</sup>, Wei Huang<sup>1,2,7†</sup>

The stabilization of black-phase formamidinium lead iodide ( $\alpha$ -FAPbI<sub>3</sub>) perovskite under various environmental conditions is considered necessary for solar cells. However, challenges remain regarding the temperature sensitivity of  $\alpha$ -FAPbI<sub>3</sub> and the requirements for strict humidity control in its processing. Here we report the synthesis of stable  $\alpha$ -FAPbI<sub>3</sub>, regardless of humidity and temperature, based on a vertically aligned lead iodide thin film grown from an ionic liquid, methylamine formate. The vertically grown structure has numerous nanometer-scale ion channels that facilitate the permeation of formamidinium iodide into the lead iodide thin films for fast and robust transformation to  $\alpha$ -FAPbI<sub>3</sub>. A solar cell with a power-conversion efficiency of 24.1% was achieved. The unencapsulated cells retain 80 and 90% of their initial efficiencies for 500 hours at 85°C and continuous light stress, respectively.

The high power-conversion efficiency (PCE) of lead halide perovskite solar cells (PSCs) is attributed to their high carrier mobility and diffusion length and adjustable bandgap of the active-layer materials (1, 2). Black-phase formamidinium lead iodide ( $\alpha$ -FAPbI<sub>3</sub>) has the narrowest bandgap (1.45 to 1.51 eV in thin films) (3, 4). This phase easily transforms into a wide-bandgap yellow nonperovskite phase ( $\delta$ -FAPbI<sub>3</sub>) under ambient conditions because the large size of FA<sup>+</sup> induces lattice distortion (5, 6), so routes have been developed to stabilize  $\alpha$ -FAPbI<sub>3</sub> perovskite thin films. Some of these approaches involve mixing alternative cations, anions, or both to form hybrid formamidinium perovskites, such as the FA<sub>x</sub>MA<sub>1-x</sub> double cation (7); the FA<sub>1-x-y</sub>MA<sub>x</sub>Cs<sub>y</sub> triple cation (8); and even FA<sup>+</sup>, MA<sup>+</sup>, Rb<sup>+</sup>, Cs<sup>+</sup>, SCN<sup>-</sup>, and Br<sup>-</sup> multiple cation-anion hybrids (5, 9, 10). Although these modifications

improve the stability and enhance PCEs (10, 11), high-quality perovskite and perovskite intermediate thin films must be processed in an inert atmosphere with strict control of both the temperature and relative humidity (RH). These requirements greatly limit production and applications of PSCs (12). The stability issues result from interactions of the precursors in their common solvents and their

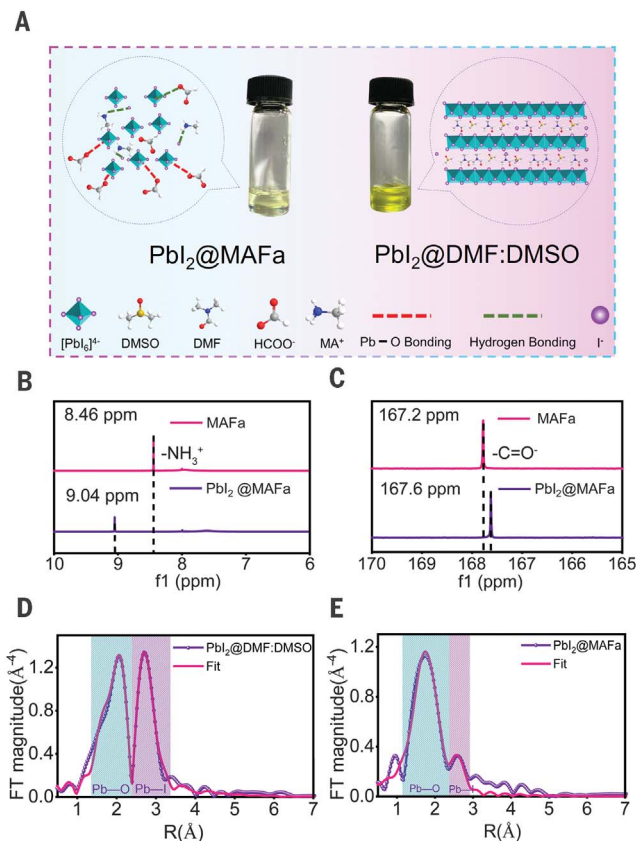
thin films. These interactions control the assembly of perovskite segments and affect the stability and performance of the frameworks (13).

We report a synthesis of stable black-phase  $\alpha$ -FAPbI<sub>3</sub> that is insensitive to environmental conditions during its preparation. Vertically aligned thin films of lead iodide (PbI<sub>2</sub>) are prepared from the ionic liquid methylamine formate (MAFa). Unlike commonly used solvents, such as *N,N*-dimethylformamide (DMF) and dimethyl sulfoxide (DMSO), strong interactions with PbI<sub>2</sub> through C=O...Pb chelation and N-H...I hydrogen bonds in the MAFa solvent promoted the vertical growth with respect to the substrate. Formamidinium iodide (FAI) could enter the PbI<sub>2</sub> thin films through in situ formation of ion channels, which notably reduced the formation energy barriers. A fast transformation to stable black-phase  $\alpha$ -FAPbI<sub>3</sub> was observed irrespective of RH (20 to 90%) and temperature (25° to 100°C). We achieved a PCE of >24% in ambient air, with 93% of the initial efficiency retained up to 5000 hours (under nitrogen-filled glove box), thermal stability for 500 hours (80% of the initial efficiency retained at 85°C), and stability under continuous light stress (90% of the initial efficiency retained over 500 hours of operation at maximum power point).

We dissolved 1.5 M PbI<sub>2</sub> in two different solvents: MAFa (fig. S1) and DMF:DMSO (9:1,

### Fig. 1. Chemical environment for precursors in different solvents.

(A) Images of PbI<sub>2</sub>@MAFa and PbI<sub>2</sub>@DMF:DMSO solutions and schematic diagram of interactions in the solutions. (B) <sup>1</sup>H NMR spectra of the two solutions before and after dissolution of PbI<sub>2</sub>. (C) <sup>13</sup>C NMR spectra of the two solutions before and after dissolution of PbI<sub>2</sub>. (D and E) Extended x-ray absorption fine structure spectra and fits in R-space at the Pb L<sub>3</sub>-edge of PbI<sub>2</sub>@DMF:DMSO (D) and PbI<sub>2</sub>@MAFa (E). The green area represents the Pb...O bond, and the purple area represents the Pb-I bond. FT, Fourier transform.



<sup>1</sup>Key Laboratory of Flexible Electronics (KLoFE) and Institute of Advanced Materials (IAM), Nanjing Tech University, 30 South Puzhu Road, Nanjing 211816, Jiangsu, China. <sup>2</sup>Frontiers Science Center for Flexible Electronics, Xi'an Institute of Flexible Electronics (IFE) and Xi'an Institute of Biomedical Materials and Engineering, Northwestern Polytechnical University, 127 West Youyi Road, Xi'an 710072, China. <sup>3</sup>Joint Key Laboratory of the Ministry of Education, Institute of Applied Physics and Materials Engineering, University of Macau, Avenida da Universidade, Taipa, Macau 999078, China. <sup>4</sup>Shanghai Synchrotron Radiation Facility (SSRF), Zhangjiang Lab, Shanghai Advanced Research Institute, Chinese Academy of Sciences, 239 Zhangheng Road, Shanghai 201204, China. <sup>5</sup>Beijing Synchrotron Radiation Facility, Institute of High Energy Physics, Chinese Academy of Sciences, Beijing 100049, China. <sup>6</sup>Department of Educational Science, Laboratory of College Physics, Hunan First Normal University, Changsha 410205, Hunan, China. <sup>7</sup>Key Laboratory for Organic Electronics and Information Displays and Institute of Advanced Materials, Nanjing University of Posts and Telecommunications, Nanjing 210023, China.

\*These authors contributed equally to this work.

†Corresponding author. Email: iamyhchen@njtech.edu.cn (Y.C.); iamwhuang@nwpu.edu.cn (W.H.)

**Table 1. Parameters of champion devices based on FAPbI<sub>3</sub>@MAFa and FAPbI<sub>3</sub>@DMF:DMSO perovskite thin films.**

Solvents	V <sub>oc</sub> (V)	J <sub>sc</sub> (mA cm <sup>-2</sup> )	FF (%)	PCE (%)
MAFa	1.17	25.34	81.36	24.1
DMF:DMSO	1.15	24.72	77.85	22.1

v/v) (Fig. 1A). The PbI<sub>2</sub> in DMF:DMSO (PbI<sub>2</sub>@DMF:DMSO) solution was a deep yellow, whereas a yellow-green solution formed in the MAFa solvent. Proton nuclear magnetic resonance (<sup>1</sup>H NMR) spectra of the two solutions before and after dissolution of PbI<sub>2</sub> (Fig. 1B) (12, 14) showed that the amino hydrogen spectrum in the MAFa solution shifted from 8.46 to 9.04 parts per million (ppm) because of amino hydrogen forming a strong N-H...I hydrogen bond with an I<sup>-</sup> ion in solution (14–16). However, no similar hydrogen-bond interactions were observed in the PbI<sub>2</sub>@DMF:DMSO solution (fig. S2). Moreover, the peak of C=O in the <sup>13</sup>C NMR spectra moved from 167.2 ppm for pure MAFa to 167.6 ppm for the PbI<sub>2</sub> in MAFa (PbI<sub>2</sub>@MAFa) solution (Fig. 1C), which is indicative of a strong interaction of the C=O group in MAFa with Pb<sup>2+</sup> (15, 17), but no clear

shift was observed before and after the dissolution of PbI<sub>2</sub> in DMF:DMSO (fig. S3).

We used x-ray absorption near-edge structure to determine the coordination environment of the Pb atoms in the two solvents. Both Pb...O and Pb-I bonds were observed in DMF:DMSO (Fig. 1D), which we attributed to the coordination of both S=O in DMSO and C=O in DMF with Pb<sup>2+</sup> (fig. S4) (13). Strong Pb-I bonds originated from the layered PbI<sub>2</sub> molecules, which indicated relatively weak interactions between the solvent and PbI<sub>2</sub> molecules. By contrast, the PbI<sub>2</sub>@MAFa solution had stronger Pb...O coordination and weaker Pb-I bonding (Fig. 1E). Moreover, the length of the Pb...O bond decreased from 2.48 to 2.35 Å (table S1) compared with that of the PbI<sub>2</sub>@DMF:DMSO solution. This observation indicated an extremely strong C=O...Pb interaction in the PbI<sub>2</sub>@MAFa solu-

tion, which plays an important role in affecting the layered structure of PbI<sub>2</sub> (14, 18).

Free I<sup>-</sup> formed hydrogen bonds with the amino groups of MAFa that could protect I<sup>-</sup> in solution from oxidation (12, 14, 19). We exposed the two solutions to the atmosphere (RH > 80%) for 6 hours; the PbI<sub>2</sub>@DMF:DMSO solution formed considerable amounts of precipitate (fig. S5) and had absorption characteristics of I<sup>3-</sup> (fig. S6), whereas a clear solution and no absorption of I<sup>3-</sup> were observed for the PbI<sub>2</sub>@MAFa solution (fig. S7) (14). We attributed the improved solution stability to strong interactions of MAFa and PbI<sub>2</sub> through C=O...Pb chelation and N-H...I hydrogen bonds.

We systematically investigated the PbI<sub>2</sub> thin film formation and crystallization processes from these solutions. The PbI<sub>2</sub>@MAFa thin films were prepared in air under ambient humidity, but the PbI<sub>2</sub>@DMF:DMSO thin films were prepared in a N<sub>2</sub>-filled glove box. A needlelike surface morphology of PbI<sub>2</sub> was observed after spin coating (0 s) from PbI<sub>2</sub>@DMF:DMSO solution (Fig. 2A), consistent with previous reports (13, 20). The needlelike initial grains provided multiple nucleation sites, which caused the grains to contract during the growth process and form undesirable pinholes.

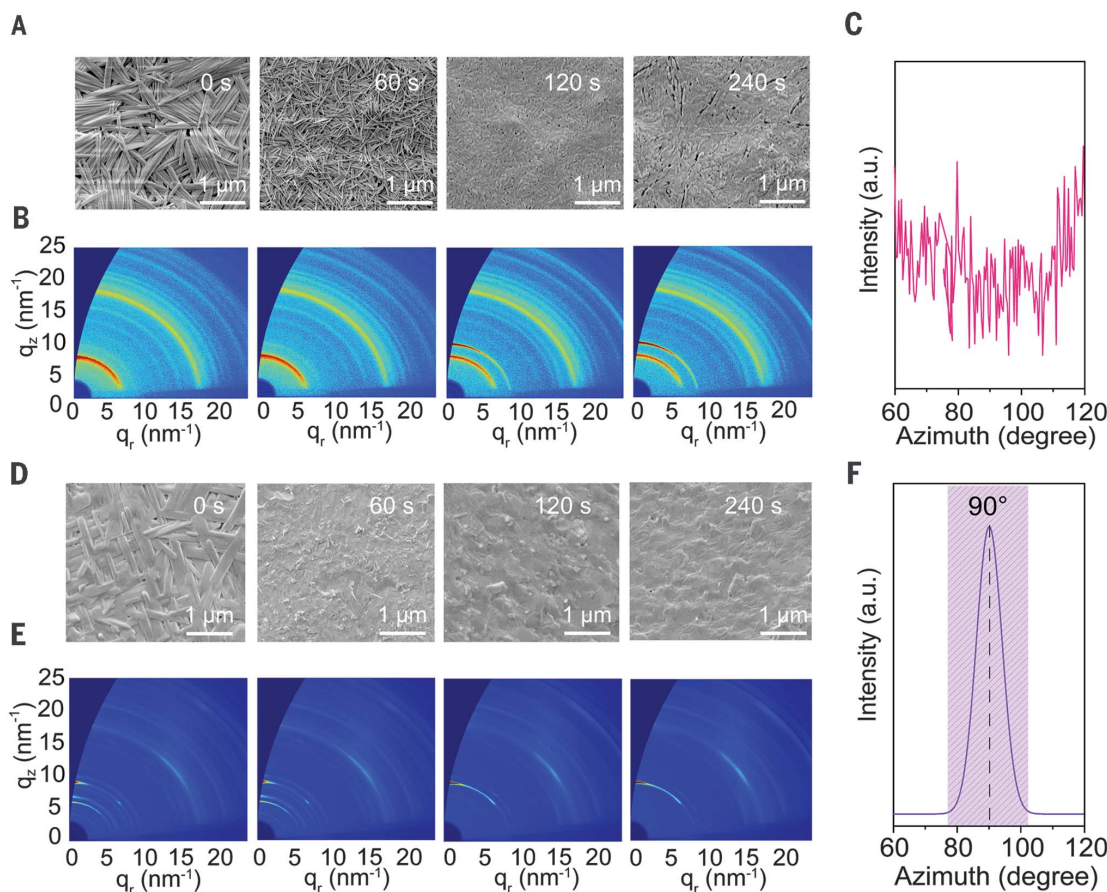


**Fig. 2. Morphology and structural characterization of PbI<sub>2</sub>@DMF:DMSO and PbI<sub>2</sub>@MAFa films.**

(A) Scanning electron microscopy (SEM) images of PbI<sub>2</sub>@DMF:DMSO films at different annealing times. (B) In situ GIWAXS spectra of PbI<sub>2</sub>@DMF:DMSO films at the corresponding annealing time. (C) Azimuth integration at  $q \approx 9.25 \text{ nm}^{-1}$  for PbI<sub>2</sub>@DMF:DMSO thin films. a.u., arbitrary units. (D) SEM images of PbI<sub>2</sub>@MAFa films at different annealing times. (E) In situ GIWAXS spectra of PbI<sub>2</sub>@MAFa films at corresponding annealing times. (F) Azimuth integration at  $q \approx 9.25 \text{ nm}^{-1}$  for PbI<sub>2</sub>@MAFa thin films.

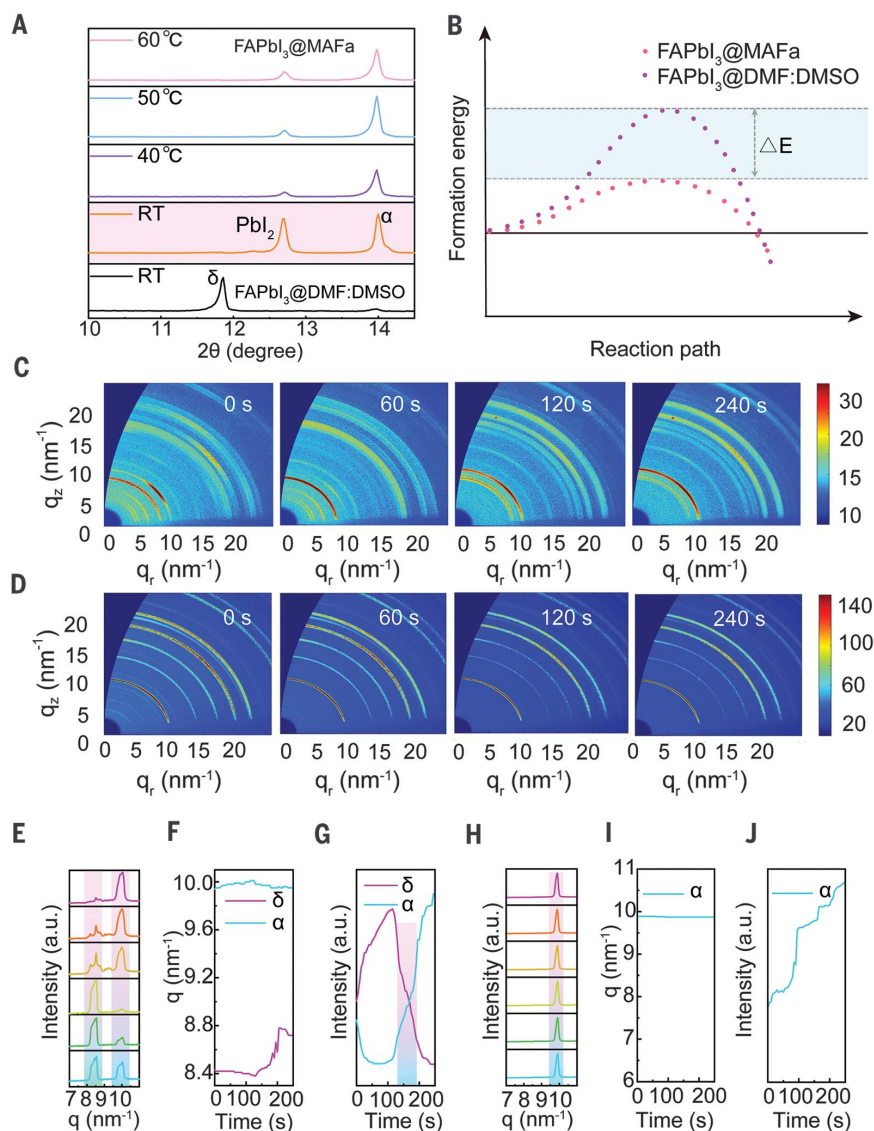


**Fig. 3. Structural characterization of FAPbI<sub>3</sub> obtained from PbI<sub>2</sub>@DMF:DMSO and PbI<sub>2</sub>@MAFa films.**

(A) XRD spectra of FAPbI<sub>3</sub> perovskite films prepared from PbI<sub>2</sub>@MAFa and PbI<sub>2</sub>@DMF:DMSO films at room temperature (RT). The FAPbI<sub>3</sub>@MAFa film was prepared under atmospheric conditions and the humidity exceeded 80%, whereas the FAPbI<sub>3</sub>@DMF:DMSO film was prepared in a nitrogen glove box because it cannot be prepared under such high humidity conditions. (B) Schematic diagram of perovskite crystallization kinetics of FAPbI<sub>3</sub> film under PbI<sub>2</sub>@MAFa (pink) and PbI<sub>2</sub>@DMF:DMSO (purple) films, respectively.  $\Delta E$ , change in energy barrier. (C and D) In situ GIWAXS spectra of FAPbI<sub>3</sub>@DMF:DMSO perovskite films (C) and FAPbI<sub>3</sub>@MAFa films (D) under different annealing times. (E) 1D GIWAXS integral spectra of FAPbI<sub>3</sub>@DMF:DMSO at different annealing times. (F) Variation of the diffraction ring of  $\alpha$ -FAPbI<sub>3</sub> and  $\delta$ -FAPbI<sub>3</sub> with annealing time for the case of PbI<sub>2</sub>@DMF:DMSO films. (G) Competition of the integrated intensity of  $\alpha$ -FAPbI<sub>3</sub> and  $\delta$ -FAPbI<sub>3</sub> with annealing time for the case of PbI<sub>2</sub>@DMF:DMSO films. (H) 1D GIWAXS integral spectra of FAPbI<sub>3</sub>@MAFa at different annealing times. (I) Variation in the diffraction ring of  $\alpha$ -FAPbI<sub>3</sub> with annealing time for the case of PbI<sub>2</sub>@MAFa films. (J) Evolution of black-phase FAPbI<sub>3</sub>@MAFa perovskite with annealing time.

To further understand the crystallization behavior of the PbI<sub>2</sub> thin films, we used in situ grazing-incidence wide-angle x-ray scattering (GIWAXS). The precursor phase (near  $q \approx 7 \text{ nm}^{-1}$ , where  $q$  is the scattering vector) was the main component of the PbI<sub>2</sub>@DMF:DMSO thin films in the initial stage of crystallization (Fig. 2B and fig. S8A). As the annealing time was prolonged,

a PbI<sub>2</sub> signal near  $q \approx 9.25 \text{ nm}^{-1}$  appeared (21). Although the diffraction intensity of PbI<sub>2</sub> increased as the annealing time was prolonged, most of the precursor structures had a strong signal. The strong Debye-Scherrer ring with an isotropic intensity distribution indicated that the grain orientation was completely random. This result was further confirmed by the disordered

integration lines, as shown by the azimuthal integration of the PbI<sub>2</sub> diffraction ring (Fig. 2C) (8, 22).

In contrast to DMF:DMSO, the use of MAFa as a solvent promoted the formation of uniform and PbI<sub>2</sub> grains larger than 1  $\mu\text{m}$  after spin coating (Fig. 2D). Notably, diffraction from MAPbI<sub>3</sub> was observed given the presence of methylamine ions in the MAFa solution (fig. S9). When the annealing time was prolonged, full coverage of pinhole-free PbI<sub>2</sub> thin films with large grains was achieved. The initial strong diffraction signal of PbI<sub>2</sub> and weak MAPbI<sub>3</sub> signal near  $q \approx 10 \text{ nm}^{-1}$  (Fig. 2E and fig. S8B) corresponded to the features in the x-ray diffraction (XRD) spectra. Although a certain precursor structure was produced at the beginning of spin coating, the precursor gradually transformed into a stable PbI<sub>2</sub> phase through a solid-solid conversion during annealing (22).

After the annealing process, the resulting PbI<sub>2</sub> thin films had a strong degree of preferential orientation with respect to the contact, as evident from sharp and discrete Bragg spots (Fig. 2E, 240 s), and the only pole figures of the azimuthal angle were at 90° without noticeable peaks along the same rings (Fig. 2F) (23). Moreover, we found the random orientation of PbI<sub>2</sub> domains in the PbI<sub>2</sub>@DMF:DMSO thin films from the high-resolution transmission electron microscopy (HRTEM) (fig. S10) (24), whereas the (001)-oriented PbI<sub>2</sub> domains have a high degree of orientation and show a very regular arrangement in the PbI<sub>2</sub>@MAFa thin films (fig. S11). This allows the formation of a regular mesoporous structure of ~5 to 10 nm between the oriented domains of PbI<sub>2</sub> with the evaporation of MAFa (fig. S11, A and B) because MAFa remains in the thin films (fig. S12). Moreover, a clear hole was observed in the side view of the PbI<sub>2</sub>@MAFa sample (fig. S11C). This structure led to vertically aligned growth of the PbI<sub>2</sub> thin films with formation of nanometer-scale ion channels between the layered PbI<sub>2</sub>, which provides a direct reaction channel for cations. This differs from the previously reported pore formation in PbI<sub>2</sub> films (25–27). Most notably, the PbI<sub>2</sub>@MAFa thin films were more stable under high humidity than the PbI<sub>2</sub>@DMF:DMSO thin films as a result of the strong Pb···O and hydrogen-bond interactions between residual MAFa and the PbI<sub>2</sub> framework (figs. S13 and S14) (14).

We prepared perovskite thin films under ambient conditions in air. The FAPbI<sub>3</sub>@DMF:DMSO thin films (prepared from PbI<sub>2</sub>@DMF:DMSO thin films at room temperature in a N<sub>2</sub>-filled glove box) had a weak  $\alpha$  phase at  $\sim 13.9^\circ$  with a strong  $\delta$ -phase signal ( $\sim 11.8^\circ$ ) because of the low formation barrier of the  $\delta$  phase (Fig. 3A) (3, 21). By contrast, no  $\delta$  phase was observed in the FAPbI<sub>3</sub>@MAFa thin films (prepared by using PbI<sub>2</sub>@MAFa thin films at

room temperature in air), but a very strong  $\alpha$ -FAPbI<sub>3</sub> perovskite signal was observed together with the PbI<sub>2</sub> peak at  $\sim 12.7^\circ$  (2I). This can be attributed to the fact that MAFA prevents the transformation of PbI<sub>2</sub> to  $\delta$ -phase perovskite by the strong interactions of MAFA and PbI<sub>2</sub> through C=O...Pb chelation and N-H...I hydrogen bonds. The phase transition temperature of  $\alpha$ -FAPbI<sub>3</sub> through the PbI<sub>2</sub>@MAFA thin films decreased considerably and allowed for the transition to take place at room temperature and in air.

This result was further confirmed by a strong absorption with a band edge at  $\sim 820$  nm and steady-state photoluminescence emission at  $\sim 820$  nm for the FAPbI<sub>3</sub>@MAFA film (fig. S15) (2). The PbI<sub>2</sub> peak intensity gradually weakened and crystallization of  $\alpha$ -FAPbI<sub>3</sub> was further promoted when the substrate temperature was increased. Moreover, the surface roughness of the perovskite films decreased from 20.5 to 10.3 nm (fig. S16) together with an increase in grain size (fig. S17) (3). The  $\delta$  phase was suppressed in the FAPbI<sub>3</sub>@MAFA thin films because the vertical crystal orientation of the PbI<sub>2</sub> structure provided nanoscale ion channels for rapid entry of FA<sup>+</sup> and reduced the energy barrier to formation of  $\alpha$ -FAPbI<sub>3</sub> (Fig. 3B) (28). The PbI<sub>2</sub>@DMF:DMSO thin films had random orientation distributions (Fig. 2C), which limit the diffusion of FA<sup>+</sup>, and this greater energy barrier to form  $\alpha$ -FAPbI<sub>3</sub> favored the formation of a low-energy yellow phase (29).

The crystallization process of the FAPbI<sub>3</sub> perovskite thin films was further monitored by in situ GIWAXS measurement in real time. Crystals of the FAPbI<sub>3</sub>@DMF:DMSO perovskite thin film grew in the vicinity of  $30^\circ$  through azimuth integration (fig. S18) and had a large  $\delta$ -FAPbI<sub>3</sub> phase near  $q \approx 8.5$  nm<sup>-1</sup> (Fig. 3C) (2I). Although the thin film eventually transformed into  $\alpha$ -FAPbI<sub>3</sub>, we could not rule out the possibility of a large amount of  $\delta$ -FAPbI<sub>3</sub> remaining (Fig. 3C, 240 s, and fig. S19). However, for the FAPbI<sub>3</sub>@MAFA perovskite thin films, stable  $\alpha$ -FAPbI<sub>3</sub> perovskite thin films formed after the deposition of FAI without annealing (Fig. 3D and fig. S20). A small amount of the intermediates and PbI<sub>2</sub> transformed into  $\alpha$ -FAPbI<sub>3</sub> perovskite structures during the annealing process, which is consistent with the XRD analysis.

Moreover, one-dimensional (1D) integration diagrams of 2D GIWAXS images (Fig. 3, E to J) indicated competition between the formation of  $\delta$ -FAPbI<sub>3</sub> and  $\alpha$ -FAPbI<sub>3</sub> phases in the case of the PbI<sub>2</sub>@DMF:DMSO thin films (13). The peak position of  $\delta$ -FAPbI<sub>3</sub> markedly shifted to a high  $q$  value upon annealing (Fig. 3F), which we attribute to the structural transformation. This process resulted in the fluctuation of the  $\alpha$ -FAPbI<sub>3</sub> peak position over a small range near  $q \approx 10$  nm<sup>-1</sup>. The integrated intensity of

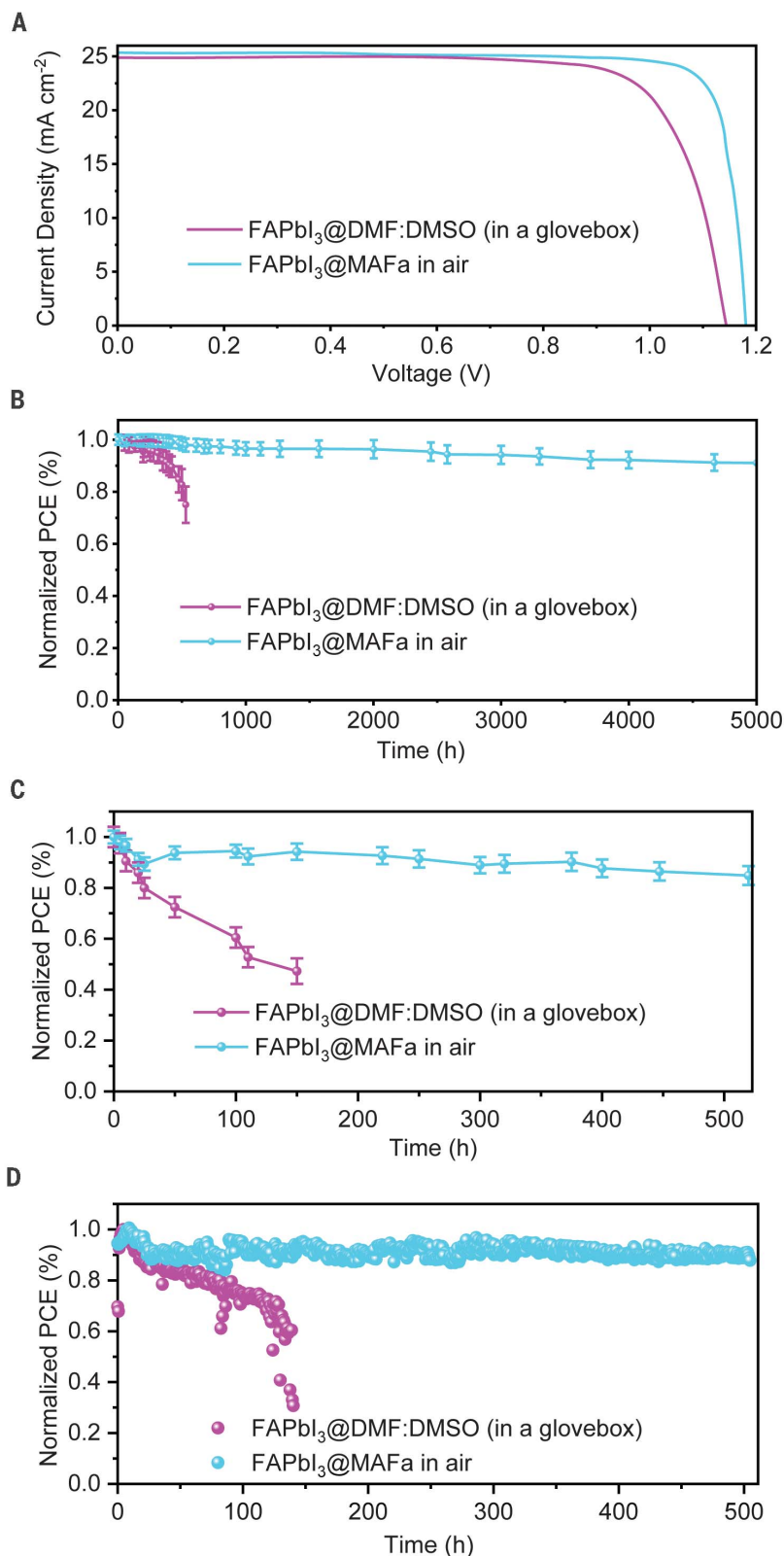


**Fig. 4. Photovoltaic device performance.** (A)  $J$ - $V$  curves of champion device based on FAPbI<sub>3</sub>@MAFA and FAPbI<sub>3</sub>@DMF:DMSO films. (B) Stability of unencapsulated devices stored in a N<sub>2</sub>-filled glove box in the dark. Error bars indicate the error or uncertainty in the reported measurements. (C) Comparison of the thermal stability of two unencapsulated devices under continuous heating at 85°C in a N<sub>2</sub>-filled glove box. Error bars indicate the error or uncertainty in the reported measurements. (D) Operational stability of two unencapsulated devices at maximum power point (0.92 and 0.72 V for FAPbI<sub>3</sub>@MAFA and FAPbI<sub>3</sub>@DMF devices, respectively) under a white light-emitting diode lamp in a N<sub>2</sub>-filled glove box.

$\delta$ -FAPbI<sub>3</sub> was markedly higher than that of  $\alpha$ -FAPbI<sub>3</sub> in the early stage of crystallization (Fig. 3G); however,  $\delta$ -FAPbI<sub>3</sub> phases remained inside the final FAPbI<sub>3</sub>@DMF:DMSO perovskite thin films (2I). By contrast, the FAPbI<sub>3</sub>@MAFa perovskite thin films maintained a stable  $\alpha$ -FAPbI<sub>3</sub> phase from the initial stage of crystallization (Fig. 3H), and the peak position remained stable (Fig. 3I). This result indicates that the FAPbI<sub>3</sub>@MAFa perovskite thin films had excellent crystallinity and a stable structure, as reflected by the increasing trend of the integrated peak intensity (Fig. 3J) (8).

Generally, the I–Pb–I ionic bonds are strong in the layered structure of PbI<sub>2</sub>, whereas the van der Waals between adjacent sandwiched layers is weak. This allows a successfully insertion of different guest molecules, bringing about the expansion of interlayer distance along the *c* axis (13, 30). Because of the large size of FA ions, it is difficult to insert them into the layered structure of PbI<sub>2</sub>. However, FAI has a high affinity for PbI<sub>2</sub> (31), and it is easy to interact with PbI<sub>2</sub> at the edge of the crystal to form a  $\delta$ -phase perovskite with a low formation energy barrier (32). The randomly arranged PbI<sub>2</sub> structure formed by the DMF:DMSO solvent could further affect the FAI diffusion process, thus resulting in the easy formation of  $\delta$ -FAPbI<sub>3</sub> perovskite. In the PbI<sub>2</sub>@MAFa thin films, ion channels are constructed that notably improve the diffusion path of FAI in the PbI<sub>2</sub> thin films, providing direct reaction channels for ions and greatly reducing the energy required to transform PbI<sub>2</sub> into  $\alpha$ -FAPbI<sub>3</sub> perovskite. In addition, because of the strong chemical effect of MAFa, the structure of PbI<sub>2</sub> changes from the original Pb–I–Pb line structure to a corner-sharing layered structure, which consists of the initial preparation of FAPbI<sub>3</sub> and MAPbI<sub>3</sub> by HPbI<sub>3</sub> (33). This corner-sharing structure prevents the transformation of PbI<sub>2</sub> into  $\delta$ -FAPbI<sub>3</sub> perovskite but facilitates the transformation of PbI<sub>2</sub> into  $\alpha$ -FAPbI<sub>3</sub> perovskite.

Moreover, because of the different growth directions of the PbI<sub>2</sub>@DMF:DMSO thin films, the diffraction peak positions of the generated  $\alpha$ -FAPbI<sub>3</sub> were located near  $q = 9.95 \text{ nm}^{-1}$ , compared with the  $\alpha$ -FAPbI<sub>3</sub> prepared from PbI<sub>2</sub>@MAFa thin films, which were fixed at  $q = 9.80 \text{ nm}^{-1}$  (fig. S21). The large FA<sup>+</sup> anion did not fit well with such a smaller interplanar spacing. This mismatch was not conducive to structural stability of the thin films and contributed to their sensitivity to humidity (figs. S22 and S23) (32, 34, 35). Because the PbI<sub>2</sub>@MAFa thin films have excellent vertically oriented crystallization, the FA<sup>+</sup> quickly enters the interior of the crystal in the second step and immediately reacts with PbI<sub>2</sub> to form a stable  $\alpha$ -FAPbI<sub>3</sub> structure. Moreover, the interaction between the perovskite framework and MAFa can probably reduce the elastic

modulus of the perovskite film, which alleviates the lattice strain inside the film and relieves the tensile stress on the surface (fig. S24). These could help to improve the stability of the FAPbI<sub>3</sub> perovskite film under high humidity (movie SI).

We prepared PSCs with a planar structure of indium tin oxide/SnO<sub>2</sub> (20 nm)/perovskite (~950 nm)/spiro-OMeTAD (80 nm)/MoO<sub>3</sub> (5 nm)/Au (100 nm). A device based on FAPbI<sub>3</sub>@MAFa perovskite thin films with a champion PCE of 24.1% was achieved, with an open-circuit voltage ( $V_{oc}$ ) of 1.17 V, a short-circuit current ( $J_{sc}$ ) of 25.34 mA cm<sup>-2</sup>, and a fill factor (FF) up to 81.36% at an RH of 80%, and the PCE was much higher than that for a PSC based on FAPbI<sub>3</sub>@DMF:DMSO perovskite thin films under a N<sub>2</sub>-filled glove box (22.12%) (Table 1). The steady-state output efficiency had a PCE close to 23.7%, and the steady-state output photocurrent density was 25.23 mA cm<sup>-2</sup> (fig. S25), which is near that obtained from the *J*-*V* curve measurements (Fig. 4A).

We compared the performance of PSCs prepared under an RH of 30, 50, 70, and 90%. Devices based on FAPbI<sub>3</sub>@DMF:DMSO perovskite thin films had an efficiency >20% at an RH of 30%, which decreased to 18% at an RH of 50%, and no photovoltaic performance was observed at an RH > 70% (fig. S26 and table S2). However, a PCE of ~23% with negligible hysteresis was achieved by the FAPbI<sub>3</sub>@MAFa thin films regardless of RH (figs. S26 to S28 and table S2). Moreover, a high PCE of 20.76% for a large-area device was achieved (1 cm by 1 cm) (fig. S29).

The trap density of the FAPbI<sub>3</sub>@MAFa perovskite thin films ( $4.74 \times 10^{15} \text{ cm}^{-3}$ ) was lower than that of FAPbI<sub>3</sub>@DMF:DMSO perovskite thin films ( $1.36 \times 10^{16} \text{ cm}^{-3}$ ) (fig. S30), which is also conducive to lower carrier recombination. This result was confirmed by the dependence of the  $V_{oc}$  on the light intensity (fig. S31) and the dependence of  $J_{sc}$  on the light intensity (fig. S32). Trap-assisted recombination and bimolecular recombination were negligible in the FAPbI<sub>3</sub>@MAFa perovskite thin films, which is consistent with its longer carrier lifetime (312.13 ns) than that of the FAPbI<sub>3</sub>@DMF:DMSO perovskite thin films (9.82 ns) (fig. S33). Moreover, the FAPbI<sub>3</sub>@MAFa thin films had more balanced carrier transport and a prolonged average lifetime owing to their high crystalline quality and low defect state density (figs. S34 and S35 and table S3), which contributed to the improved stability and current density of the devices.

The long-term stability of the PSCs was tested under various conditions without encapsulation. The FAPbI<sub>3</sub>@MAFa device retained 93% of its original PCE after storage in the N<sub>2</sub>-filled glove box for 5000 hours. This result contrasts with that of the FAPbI<sub>3</sub>@DMF:DMSO device, which underwent a 30% PCE loss within only 500 hours (Fig. 4B). More-

over, we conducted the device thermal stability at 85°C in a N<sub>2</sub>-filled glove box (Fig. 4C) (36) and found that the average PCE of the FAPbI<sub>3</sub>@MAFa device remained at 80% of the initial efficiency for ~500 hours in a N<sub>2</sub>-filled glove box, whereas serious PCE decrease was observed in the FAPbI<sub>3</sub>@DMF:DMSO device, with 45% left after only ~150 hours. In addition, we performed the stability under operational conditions examined at the maximum power point. As seen in Fig. 4D, the FAPbI<sub>3</sub>@DMF:DMSO device degrades rapidly, with 60% decrease of its initial efficiency within 140 hours. By contrast, the FAPbI<sub>3</sub>@MAFa device retains 90% of its initial efficiency for 500 hours. We attribute the greater stability of the PbI<sub>2</sub>@MAFa thin films to the vertically oriented crystal growth that provides ion channels for the rapid reaction in the second step, which created stable  $\alpha$ -FAPbI<sub>3</sub> perovskite thin films. Also, residual MAFa protected the thin films from erosion by water and oxygen and combined with Pb vacancies at grain boundaries to prevent the decomposition of the thin films (fig. S36).

## REFERENCES AND NOTES

- National Renewable Energy Laboratory, Best Research-Cell Efficiency Chart (US Department of Energy, 2021); [www.nrel.gov/pv/cell-efficiency.html](http://www.nrel.gov/pv/cell-efficiency.html).
- H. Min *et al.*, *Science* **366**, 749–753 (2019).
- G. Kim *et al.*, *Science* **370**, 108–112 (2020).
- J. M. Frost *et al.*, *Nano Lett.* **14**, 2584–2590 (2014).
- H. Lu *et al.*, *Science* **370**, eabb8985 (2020).
- W. S. Yang *et al.*, *Science* **348**, 1234–1237 (2015).
- N. J. Jeon *et al.*, *Nature* **517**, 476–480 (2015).
- M. Qin *et al.*, *Adv. Mater.* **31**, e1901284 (2019).
- T. Duong *et al.*, *Adv. Energy Mater.* **7**, 1700228 (2017).
- M. Saliba *et al.*, *Science* **354**, 206–209 (2016).
- M. I. Saidaminov *et al.*, *Nat. Energy* **3**, 648–654 (2018).
- L. Chao *et al.*, *Chem* **5**, 995–1006 (2019).
- Y. Guo *et al.*, *J. Am. Chem. Soc.* **137**, 15907–15914 (2015).
- X. Wang *et al.*, *Angew. Chem. Int. Ed.* **59**, 13354–13361 (2020).
- B. Li *et al.*, *Nat. Commun.* **9**, 1076 (2018).
- A. Abate *et al.*, *Nano Lett.* **14**, 3247–3254 (2014).
- A. Q. Alanazi *et al.*, *J. Am. Chem. Soc.* **141**, 17659–17669 (2019).
- J. Pan *et al.*, *Adv. Mater.* **28**, 8309–8314 (2016).
- H. Ren *et al.*, *Nat. Photonics* **14**, 154–163 (2020).
- Q. Li *et al.*, *Adv. Mater.* **30**, 1803095 (2018).
- Y. Liu *et al.*, *Angew. Chem. Int. Ed.* **59**, 15688–15694 (2020).
- T. Miyadera *et al.*, *Nano Lett.* **15**, 5630–5634 (2015).
- W. Hui *et al.*, *Nano Energy* **73**, 104803 (2020).
- T. J. Jacobsson *et al.*, *J. Am. Chem. Soc.* **138**, 10331–10343 (2016).
- X. Duan *et al.*, *Adv. Mater.* **32**, e2000617 (2020).
- H. Zhang *et al.*, *Adv. Energy Mater.* **5**, 1501354 (2015).
- C.-H. Chiang, C.-G. Wu, *Nat. Photonics* **10**, 196–200 (2016).
- Y. Zhao *et al.*, *Adv. Mater.* **32**, e1907769 (2020).
- Y. Zhao *et al.*, *Nat. Commun.* **9**, 1607 (2018).
- Y. Jo *et al.*, *Adv. Mater. Interfaces* **3**, 1500768 (2016).
- A. Binek, F. C. Hanusch, P. Docampo, T. Bein, *J. Phys. Chem. Lett.* **6**, 1249–1253 (2015).
- B. W. Park, S. I. Seok, *Adv. Mater.* **31**, e1805337 (2019).
- S. Pang *et al.*, *J. Am. Chem. Soc.* **138**, 750–753 (2016).
- T. Chen *et al.*, *Sci. Adv.* **2**, e1601650 (2016).
- Q. Han *et al.*, *Adv. Mater.* **28**, 2253–2258 (2016).
- Q. Jiang *et al.*, *Nat. Photonics* **13**, 460–466 (2019).

## ACKNOWLEDGMENTS

Y.C. acknowledges X. Huang from Nanjing Tech University (China) for assisting with HRTEM sample preparation and measurement

and for the discussion of the structure of lead iodide. **Funding:** The authors acknowledge the Natural Science Foundation of China (grants 51602149, 61705102, 91833304, and 91733302); the Natural Science Foundation of Jiangsu Province for Distinguished Young Scholars, China (grant BK20200034); the National Key Research and Development Program of China (grant 2017YFA0403400); Projects of International Cooperation and Exchanges NSFC (51811530018); the Young 1000 Talents Global Recruitment Program of China; the Jiangsu Specially-Appointed Professor Program and the "Six talent peaks" Project in Jiangsu Province, China; and the Scientific Research Fund of Hunan Provincial Education Department (20B121). **Author contributions:** Y.C. and W.Huang conceived the idea and designed the experiments. Y.C. and W.Huang supervised the work. W.Hui, L.C.,

and H.L. carried out the device fabrication and characterizations. F.X., Q.W., B.L., and Z.S. also contributed to device fabrication. Q.W., G.X., T.N., L.T., W.S., X.R., P.L., and H.Z. conducted the optical spectra measurements. H.L., B.D., and Y.X. synthesized the MAFA. D.L., Y.W., and H.D. carried out the NMR and Fourier transform infrared spectra measurements. S.Z. and J.Z. conducted the x-ray absorption fine structure measurements and analyzed the data. GIWAXS was performed and analyzed by W.Hui, Z.S., C.R., L.S., and X.G., supported by the BL14B beamline of SSRF. W.Hui and L.C. wrote the first draft of the manuscript. Y.C., Y.X., Z.W., and W.Huang participated in data analysis and provided major revisions. All authors discussed the results and commented on the manuscript.

**Competing interests:** The authors declare no competing financial or nonfinancial interests. **Data and materials availability:** All data

needed to evaluate the conclusions in the paper are present in the paper or the supplementary materials.

#### SUPPLEMENTARY MATERIALS

[science.sciencemag.org/content/371/6536/1359/suppl/DC1](https://science.sciencemag.org/content/371/6536/1359/suppl/DC1)  
Materials and Methods  
Figs. S1 to S36  
Tables S1 to S3  
References (37–47)  
Movie S1

17 November 2020; accepted 26 February 2021  
10.1126/science.abf7652

## Stabilizing black-phase formamidinium perovskite formation at room temperature and high humidity

Wei Hui, Lingfeng Chao, Hui Lu, Fei Xia, Qi Wei, Zhenhuang Su, Tingting Niu, Lei Tao, Bin Du, Deli Li, Yue Wang, He Dong, Shouwei Zuo, Bixin Li, Wei Shi, Xueqin Ran, Ping Li, Hui Zhang, Zhongbin Wu, Chenxin Ran, Lin Song, Guichuan Xing, Xingyu Gao, Jing Zhang, Yingdong Xia, Yonghua Chen and Wei Huang

*Science* **371** (6536), 1359-1364.  
DOI: 10.1126/science.abf7652

### Perovskite synthesis out in the open

Although methods have been developed that create the photoactive black perovskite phase of formamidinium lead iodide ( $\alpha$ -FAPbI<sub>3</sub>), these routes are temperature and humidity sensitive and less compatible with large-scale solar cell production. Hui *et al.* report an alternative route in which vertically aligned lead iodide thin films are grown from the ionic liquid methylamine formate. Nanoscale channels in the films lower the barrier to permeation of formamidinium iodide and enable transformation to  $\alpha$ -FAPbI<sub>3</sub>, even at high humidity and room temperature. Solar cells made with these films have power conversion efficiencies as high as 24.1% that display high stability.

*Science*, this issue p. 1359

#### ARTICLE TOOLS

<http://science.sciencemag.org/content/371/6536/1359>

#### SUPPLEMENTARY MATERIALS

<http://science.sciencemag.org/content/suppl/2021/03/24/371.6536.1359.DC1>

#### REFERENCES

This article cites 46 articles, 7 of which you can access for free  
<http://science.sciencemag.org/content/371/6536/1359#BIBL>

#### PERMISSIONS

<http://www.sciencemag.org/help/reprints-and-permissions>

Use of this article is subject to the [Terms of Service](#)

---

*Science* (print ISSN 0036-8075; online ISSN 1095-9203) is published by the American Association for the Advancement of Science, 1200 New York Avenue NW, Washington, DC 20005. The title *Science* is a registered trademark of AAAS.

Copyright © 2021 The Authors, some rights reserved; exclusive licensee American Association for the Advancement of Science. No claim to original U.S. Government Works